Available online at www.sciencedirect.com

ScienceDirect

Acta Materialia 80 (2014) 94–106

Acta MATERIALIA

www.elsevier.com/locate/actamat

Intrinsic and extrinsic size effects in the deformation of amorphous CuZr/nanocrystalline Cu nanolaminates

Wei Guo [a], Eric Jägle [a], Jiahao Yao [b,e,*], Verena Maier [c], Sandra Korte-Kerzel [c,d], Jochen M. Schneider [e], Dierk Raabe [a,*]

[a] Department of Microstructure Physics and Alloy Design, Max-Planck Institut für Eisenforschung, Düsseldorf 40237, Germany
[b] Shenyang National Laboratory for Materials Science, Institute of Metal Research, Chinese Academy of Sciences, Shenyang 110016, China
[c] Lehrstuhl für Allgemeine Werkstoffeigenschaften, FAU Erlangen-Nürnberg, Erlangen 91058, Germany
[d] Institut für Metallkunde und Metallphysik, RWTH Aachen University, Aachen 52074, Germany
[e] Lehrstuhl für Werkstoffchemie, RWTH Aachen University, Aachen 52074, Germany

Received 31 March 2014; received in revised form 20 June 2014; accepted 12 July 2014
Available online 24 August 2014

Abstract

Introducing a soft crystalline phase into an amorphous alloy can promote the compound's ductility. Here we synthesized multilayered nanolaminates consisting of alternating amorphous $Cu_{54}Zr_{46}$ and nanocrystalline Cu layers. The Cu layer thickness was systematically varied in different samples. Mechanical loading was imposed by nanoindentation and micropillar compression. Increasing the Cu layer thickness from 10 to 100 nm led to a transition from sharp, cross-phase shear banding to gradual bending and co-deformation of the two layer types (amorphous/nanocrystalline). Specimens with a sequence of 100 nm amorphous $Cu_{54}Zr_{46}$ and 50 nm Cu layers show a compressive flow stress of 2.57 ± 0.21 GPa, matching the strength of pure CuZr metallic glass, hence exceeding the linear rule of mixtures. In pillar compression, 40% strain without fracture was achieved by the suppression of percolative shear band propagation. The results show that inserting a ductile nanocrystalline phase into a metallic glass prevents catastrophic shear banding. The mechanical response of such nanolaminates can be tuned by adjusting the layer thickness.

Keywords: Nanolaminates; Metallic glass; Nanotwins; Shear band

1. Introduction

The plastic deformation of metallic glasses profoundly differs from that of crystalline materials due to the absence of long-range atomic periodicity. While plasticity of crystals is mainly achieved by dislocations, metallic glass is deformed through shear transformation zones [1] and shear bands [2]. Shear bands nucleate and propagate unpredictably upon yielding, accompanied by strain softening and catastrophic failure [3]. This impedes the widespread use of metallic glasses as structural materials, even though they possess some superior physical [4], chemical [5,6] and mechanical properties such as high strength [7,8] and high hardness [9] when compared to crystalline matter.

An important approach to increasing the ductility of a metallic glass is to introduce a softer crystalline phase into it [1]. This approach works for Zr-based [10] and Cu-based [11] bulk metallic glasses. The soft crystalline phase is assumed to act as an absorber for deformation localization. It arrests the shear band and disperses the stress, either by dislocation slip or phase transformation. However, a systematic study of the effects of size, shape and volume fraction of the soft crystalline phase on the shear band controlled deformation has not been conducted due to

* Corresponding authors. Tel.: +49 02116792333.
E-mail addresses: jhyao@imr.ac.cn (J. Yao), d.raabe@mpie.de (D. Raabe).

http://dx.doi.org/10.1016/j.actamat.2014.07.027
1359-6454/

the difficulty of synthesizing well-defined amorphous/crystalline composites.

Another way to enhance the plastic deformation of metallic glasses, besides inserting crystalline portions, is shape confinement: A decrease in the aspect ratio of the sample (i.e. samples with small dimensions in the directions perpendicular to the applied load) generates interacting, deflected shear bands with a wavy shape [12]. Previous works revealed the role of shape confinement in plasticity enhancement [13] or even fracture prevention [12,14]. It was also found that reducing the sample size changes the deformation mode of metallic glasses at the sub-micrometer scale [15]. Instantaneous propagation of shear bands can be effectively suppressed, resulting in a transition from highly localized shear banding to more homogeneous deformation under uniaxial compression. For example, a Zr-based metallic glass has been reported to be "strong yet ductile" when probed at pillar size diameters of 100 nm [16]. Such apparent strength increase of metallic glasses by size reduction can also originate from experimental factors. Therefore, these phenomena require more clarification.

Some pure nanocrystalline (nc) materials probed in sub-micron scale mechanical experiments indeed exhibit a different trend. For example, Jang and Greer [17] studied Ni pillars with a grain size of 60 nm and micro-pillar diameters between 600 and 2500 nm. They found that pillars followed a "smaller is weaker" trend, caused by the increasing surface-dominated dislocation motion. They attributed this to a transition from dislocation-driven deformation in larger pillars to grain-boundary-mediated deformation in smaller pillars. In view of these two different observations, the question arises whether the deformation behavior is dominated by the nc phase or by the glassy phase in the case of a composite containing both glassy and nc portions at the sub-micron scale.

These two ideas, namely promoting ductilization by amorphous–crystalline composite design and by size control, motivated us to synthesize a multilayered glass-containing composite with confined metallic glass fractions. The aim is to investigate the mechanical response and the governing deformation mode of such materials at the sub-micron scale.

Recently, investigations on such amorphous/nanocrystalline (am/nc) CuZr/Cu multilayers (also referred to as nanolaminates) have attracted considerable interest [18–22]. These earlier works showed that the phase fractions can be tuned by controlling the layer thickness. For example, Kim et al. [20] studied 112 nm CuZr/16 nm nc Cu multilayers and found an enhanced maximum strength by adding nc Cu layers. Liu et al. [19] found that 500 nm CuZr/500 nm Cu nanolaminates exhibit a strong barreling effect (preferential deformation) of the nc Cu layers, whereas 100 nm CuZr/100 nm Cu nanolaminates showed higher strain compatibility. Zhang et al. [18] deformed CuZr/Cu (am/nc) nanolaminate pillars with equal layer thickness from 5 to 50 nm and observed a transition from pronounced shear-banding to homogeneous deformation with increasing layer thickness. The above studies revealed that a multilayer structure consisting of an amorphous and a crystalline phase may suppress percolative and hence catastrophic shear bands and enable plastic co-deformation of the abutting phases if the layer thickness is carefully tuned. While it is clear that changing the layer thickness allows optimizing the mechanical response, the underlying reason for the optimal thickness of the layers has yet to be identified. Additionally, in crystalline/crystalline nanolaminates it was found that the yield stress increases when the layer thickness decreased due to "confined layered slip" [23]. In the am/nc case, however, modifying the Cu layer thickness changes not only the stress in the Cu layer but also the stress state in the glassy phase fraction. The influence of the nc Cu layer thickness on the shear band morphology at small length scales is not yet clarified and will be also addressed in this work.

Therefore, in this work, amorphous CuZr/nc Cu nanolaminates with varying Cu layer thickness were synthesized. We first used nanoindentation testing to study the mechanical response of these multilayers. Also, we fabricated micron- and submicron-scale pillars to study the effect of the crystalline (Cu) layer thickness on the deformation behavior of these nanolaminates. Based on the experimental observations, we study the deformation behavior as a function of the intrinsic Cu layer thickness and also of the extrinsic pillar size effect.

2. Experimental procedures

2.1. Material synthesis of the am/nc laminates

Amorphous CuZr/nc Cu nanolaminates were deposited on Si (100) wafers by direct current magnetron sputtering. Targets of pure Cu (99.99%) and Zr (99.99%), each 5.08 cm in diameter, were used to deposit alternating layers of amorphous CuZr layer and pure nc Cu layers. The base pressure was $\leqslant 10^{-7}$ mbar and the processing pressure was 3×10^{-3} mbar using pure Ar gas. The substrate rotated at a frequency of 10 min^{-1}. Three kinds of nanolaminates with different layer thickness were prepared, namely, 100 nm CuZr (amorphous)/10 nm nc Cu (referred to as MS10), 100 nm CuZr (amorphous)/50 nm nc Cu (MS50) and 100 nm CuZr (amorphous)/100 nm nc Cu (MS100). The total stacked thickness of the CuZr/Cu multilayer compounds is ~1200 nm with an amorphous CuZr cap layer. The structure of the as-deposited thinfilms was characterized by X-ray diffraction (XRD; Bruker D8 diffractometer), field-emission scanning electron microscopy (SEM; FEI Helios Nanolab 600) and transmission electron microscopy (TEM;J EOL JEM-2200FS).

2.2. Nanoindentation tests

The hardness and indentation modulus of the multilayers were measured with a diamond Berkovich indenter tip

in conjunction with a load and depth sensing nanoindenter system (Hysitron TriboIndenter 800). The indentation depth amounted to ~5–15% of the total film thickness. A minimum of 12 indents were performed on each specimen to obtain averages and standard deviations for hardness and reduced modulus. Fused silica was employed for tip area function calibration according to the method of Oliver and Pharr [24]. The Young's modulus of the (100) Si substrate assumed in the analysis is 130 GPa [25] and its Poisson's ratio is $v_{si} = 0.278$ [26]. From the literature [27,28], the Young's modulus of nc Cu is taken as 108–128 GPa and that of pure CuZr metallic glass as 84 GPa. The Young's modulus of the sputtered CuZr/Cu multilayers, as determined by using King's method [29] was ~100 GPa. The value varied slightly with the thickness of the Cu layer, i.e. 100 ± 2 GPa for MS10 and MS50 and 98 ± 2 GPa for MS100, respectively.

2.3. Micropillar compression tests

To explore the mechanical properties of the multilayers, pillars with initial diameters (Φ) between ~300 and ~2000 nm were fabricated using a dual-beam focused ion beam (FIB) system (FEI Helios Nanolab 600) operated at a final beam current of 86 pA and a constant accelerating voltage of 30 kV. The pillars were inside a 25 μm-diameter crater, leaving enough space for the 10 μm-diameter diamond flat punch to avoid simultaneous contact with surrounding bulk and the pillar. The pillar compression tests were conducted in a nanoindentation system (MTS nanoindenter G200). In order to achieve an approximately constant strain rate in the elastic regime up to the yield point, the loading rate for each pillar was scaled with its diameter to give a constant engineering stress increase rate of 7×10^4 Pa s^{-1} with loading rates ranging from 6 to 300 μN s^{-1}. The displacement during the compression was recorded at a frequency of 50 Hz. After reaching the preset maximum displacement, a 10 s holding segment followed. Unloading was done at the same rate as loading. The morphology of the pillars after deformation was further examined by SEM.

The engineering stress, $\sigma = F/A_0$, was calculated from the measured force F and the pillar cross-sectional area A_0 at 20% of its height away from the top of the pillar (deformation was confined to the top due to the tapered geometry). To avoid an ambiguous determination of a first deviation from linear elasticity (yield stress) and reduce the influence of early plasticity and the artificial, i.e. geometric, work-hardening due to the tapered geometry, we select 5% plastic strain as a compromise to determine the flow stress. For calculating the engineering strain, the displacement was firstly corrected by using Eq. (1) [30,31]:

$$L = L_{meas} - \frac{(1 - v_i^2)P}{E_i d_i} - \frac{(1 - v_{si}^2)}{E_{si} d_{si}} \quad (1)$$

where P is the applied load and d_i and d_{si} are the diameters of the pillar top and bottom, respectively. E_i and E_{si} are the Young's modulus of diamond (1220 GPa [32]) and of the (100) Si substrate (130 GPa [25]), respectively. $V_i \approx 0.2$ and $V_{si} = 0.278$ [26] are the Poisson's ratio of diamond and of the Si substrate, respectively. The engineering strain is obtained by dividing the corrected displacement over the film thickness.

3. Experimental results

3.1. Microstructure analysis

The XRD patterns of the as-deposited CuZr/Cu nanolaminates (see Fig. 1) reveal that the thickness increase of the Cu layers matches the intensity increase of the Cu (111), Cu (200) and Cu (222) peaks. Comparing the ratio of the (200) and (222) XRD intensities in the CuZr/Cu nanolaminates with that in pure Cu shows that the as-deposited layers are textured with a majority of the crystals oriented with their {111}-planes in the layer plane. This is confirmed by selected area diffraction patterns (SADP, see inset in Fig. 2a). The extra (111) spots in reciprocal space indicate the existence of nanotwins. Cross-sectional microstructures of the nanolaminates were examined in detail. A representative bright field TEM micrograph of MS50 (Fig. 2a) shows a drastic contrast difference between the amorphous CuZr layer and the nc Cu layer, clearly revealing the layered structure. The double spots around (111) in the inset SADP and fringes in the dark grains (the ones in Bragg condition) indicate (111) nanotwins in the as-deposited state, which is common in magnetron sputtered Cu thin films [33]. High resolution TEM images (Fig. 2b) show that neither crystalline phases in the amorphous layer nor transitional crystalline structures at the am/nc interfaces are present. The chemical composition of the materials was determined by atom probe tomography (LEAP 3000X HR, Cameca Instruments). The results show that the Cu concentration is 54.2 ± 0.3 at.% in the amorphous CuZr layer and 99.2 ± 0.5 at.% in the nc Cu layer.

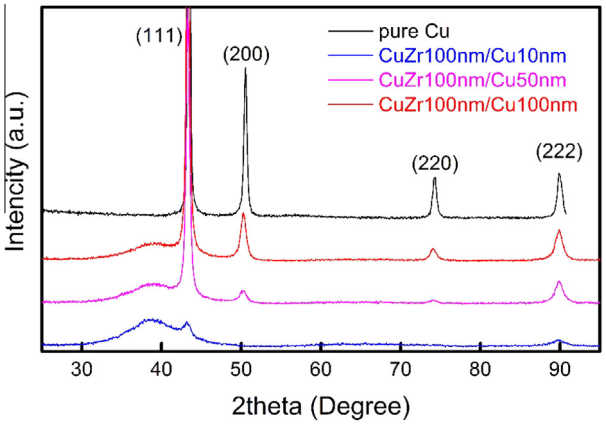

Fig. 1. XRD patterns ... for the amorphous (am) CuZr/nanocrystalline (nc) Cu nanolaminates ... and the pure Cu film.

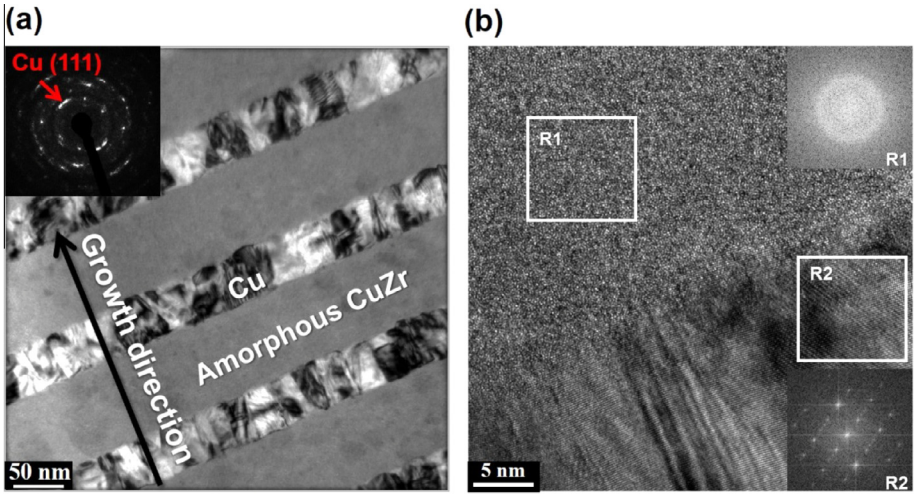

Fig. 2. Representative TEM image (a) and HRTEM image (b) of 100 nm amorphous CuZr/50 nm nc Cu nanolaminates. The SADP inset in panel (a) reveals the existence of a (1 1 1) texture and nanotwins in the Cu layers in the as-deposited state. The insets in panel (b) show the fast Fourier transform (FFT) from two regions of interest, R1 (in the amorphous layer) and R2 (in the nc layer).

3.2. Nanoindentation results for the am/nc laminates

Representative loading/unloading curves and the corresponding hardness of the am/nc CuZr/Cu nanolaminates are summarized in Fig. 3 for different penetration depths. No obvious "pop-in" (strain burst) events were detected in the load–displacement curves, indicating that no catastrophic shear bands occur during loading [22]. Table 1 summarizes the nominal hardness values derived from ~10% penetration depth of the film thickness (data from 3 mN load). We find the trend of a decreasing hardness level as a function of an increasing Cu layer thickness and Cu volume fraction in the laminates.

The cross-sectional samples of MS10 and MS50 after 5 mN indentation were cut by FIB for subsequent SEM and TEM probing. Fig. 4 shows a series of micrographs with increasing magnification in the indented sample MS10. Fig. 4a shows, as marked by red arrows, that the glass layers are locally deformed along the plane of maximum shear load. The localized stress cannot be dissipated by the top Cu layer alone; hence the load is transmitted to the layers beneath. The layered morphology remains intact along the shear plane, with no apparent discontinuities or cracks. This indicates that even Cu layers with only 10 nm thickness can suppress catastrophic shear band failure of the metallic glass matrix. This is fully consistent with the observed absence of pop-in or pronounced strain burst events when the MS10 samples are subjected to nanoindentation. The Cu layer away from the kinked region undergoes a strain below ~0.3 in the layer thickness direction, while the strain around the kinked region is above 0.8 in layer thickness direction. Fig. 4c shows a higher resolution image of this sheared region: the Moiré fringes [34] indicate that there are many dislocations located in this region, accommodating the shear, and that the Cu layer is preferentially thinned. However, for the unstrained portion of the nc Cu layer next to the shear band, the thickness remains ~10 nm, suggesting that intra-layer slip in Cu does not contribute much to the overall laminate deformation.

Fig. 5 shows a cross-sectional TEM micrograph of sample MS50 after 5 mN loading. In contrast to sample MS10, no plastic instability was observed. Instead, the Cu layer tends to rotate to comply with the local load. Apparently, the two different layers were co-deformed, as shown by the thickness reduction of both the nc Cu and the amorphous layer in Fig. 5b. The variance in thickness reduction at different positions arises from the inhomogeneous deformation state below indents. The absence of preferential thinning of the Cu layers and the absence of shear bands indicate a homogeneous deformation of the CuZr layer for this sample.

3.3. Pillar compression testing of the am/nc laminates

3.3.1. Intrinsic size effects

Fig. 6d shows the engineering stress–strain curves from the pillar compression tests for the three sample types. From the literature, the stress–strain curves of a fully amorphous homogeneous CuZr pillar [18] and of a fully nc Cu pillar [35] are also shown for comparison. Sample MS10 reveals pronounced discrete plastic strain bursts, a behavior typical of sub-micron metallic scale pillars [36] and of metallic glasses strained at room temperature [37]. Here three short strain bursts are indicative of the propagation of shear bands or the repeated propagation of one shear band [38]. The bands extend from the top of the pillars, owing to their tapered geometry (top 600 nm, bottom 800 nm). These shape-driven shear bands can propagate and penetrate the Cu and the amorphous CuZr layers, Fig. 6a.

The compressed MS50pillar shows only two well-defined shear bands nucleated in the amorphous layer. They do not penetrate the underlying Cu layer but remain confined inside the amorphous zone. Accordingly, the

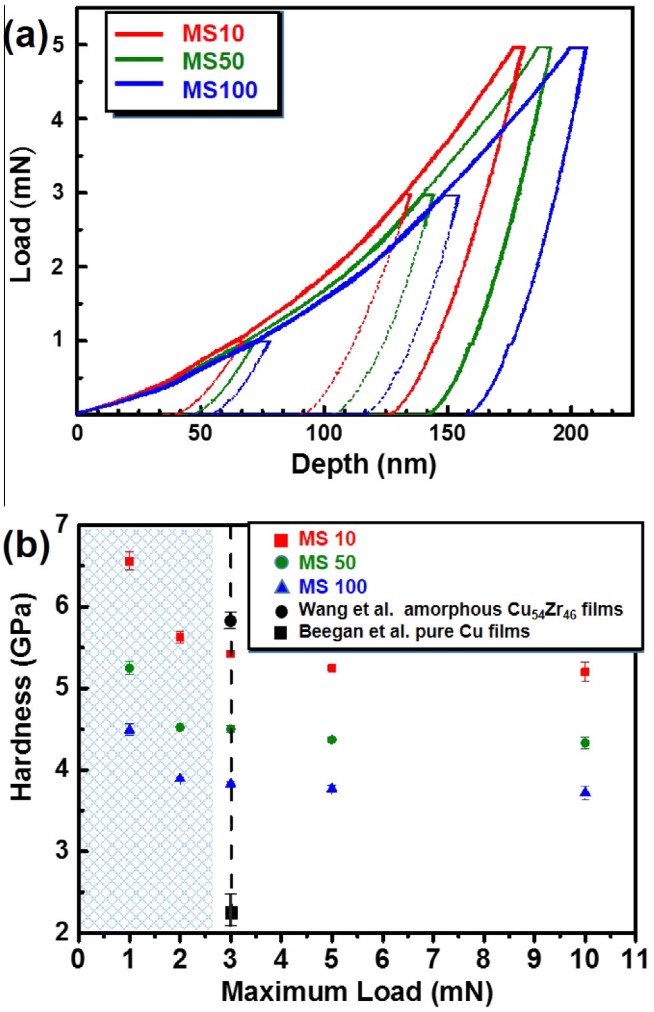

Fig. 3. (a) Nanoindentation load–displacement curves for three different CuZr/Cu nanolaminates: MS10 (100 nm amorphous CuZr/10 nm nc Cu), MS50 (100 nm amorphous CuZr/50 nm nc Cu) and MS100 (100 nm amorphous CuZr/100 nm nc Cu). (b) Plot of loading hardness vs. indentation maximum load for the same three CuZr/Cu nanolaminates. Also shown in this figure are published nanoindentation hardness values of an amorphous $Cu_{54}Zr_{46}$ film [9] and a nc Cu film.

Table 1
Hardness measured by Berkovich indentation in different nanolaminate systems: MS10 (100 nm amorphous CuZr/10 nm nc Cu); MS50 (100 nm amorphous CuZr/50 nm nc Cu); and MS100 (100 nm amorphous CuZr/100 nm nc Cu).

Material system	MS10	MS50	MS100
Hardness (GPa)	5.42 ± 0.03	4.50 ± 0.04	3.83 ± 0.03

stress–strain curve does not show significant strain bursts, Fig. 6d. This means that each shear band event in sample MS50 released less elastic stored energy than a corresponding event in sample MS10. We choose the stress at 5% plastic strain to compare the flow stress of different material systems. Interestingly, the flow stress of sample MS50 is comparable with that of sample MS10, indicating that the amorphous/crystalline interfaces are characterized by a certain strengthening plus confinement effect.

Sample MS100 has a flow stress of 1.72 GPa, mainly due to preferential deformation of the Cu layers, as revealed by their slight individual barreling, Fig. 6c. As the strain increases, strong work-hardening occurs, due to the high work-hardening capacity of nc Cu. Also, the topmost amorphous CuZr layer deformed homogeneously, expanding its diameter from ~600 to ~700 nm. When compared to the stress–strain curve of the nc Cu pillars (data taken from Ref. [35]), the MS100 nanolaminate pillar shows no significant strain bursts, indicating more homogeneous deformation of the latter sample. Although the flow stress of the MS100 pillar is below that of the samples MS10 and MS50, it is still much higher than that of pure nc Cu, Fig. 6d.

3.3.2. Extrinsic size effects

2 μm diameter pillars were fabricated for each of the multilayer samples. Fig. 7 shows a 52° tilted SEM image of the 2 μm diameter pillars deformed to ~40% strain (MS50, MS100). Sample MS50 shows multiple shear bands at the pillar surface, Fig. 7a. Most of the shear bands are either deflected or "captured" by the Cu layers, but a few of the bands penetrate through multiple layers. Accordingly, the plateau after yielding in the stress–strain curve (stage II in Fig. 7d) indicates that there is no work-hardening during further plastic deformation. For sample MS100, there are no visible shear bands on the entire pillar surface. As the deformation of the pillar increases, barreling of the entire nanolaminate occurs, but there is no obvious extrusion of the copper layers. This indicates that no preferential deformation of the nc Cu layers takes place.

Fig. 8 shows the effect of the pillar diameter on the deformation behavior of the three types of nanolaminates. For the MS10 pillars, Fig. 8a–c shows that few large shear bands control the deformation of the pillars for all sizes. For the smallest MS50 and MS100 pillars (300 nm, Fig. 8d and g), strong barreling of the Cu layers is observed. However, the barreling of the Cu layers decreases with the increase in pillar size, suggesting more deformation and dislocation interactions within the Cu layer and also enhanced strain compatibility between the nc and amorphous layers. For larger pillar sizes (900 nm, Fig. 8f), the shear bands are either deflected or absorbed by the underlying Cu layers. More confined shear bands with length scales close to the amorphous layer thickness are formed for strain accommodation. For the large pillars in the MS100 samples, the absence of shear steps and the diameter changes after deformation indicate a more homogeneous co-deformation [11–13].

The compressive stress–strain curves for the pillar compression tests are shown in Fig. 9. The strong barreling observed for the large pillars and the associated increase in the cross-sectional area lead to a high unloading modulus and will not be further analyzed here. However, the flow stress values taken at 5% flow strain are rather reliable in describing the stress state of the pillars. When the pillar diameter is reduced from 2000 to 750 nm, the flow stress of the MS10 pillars firstly decreased from 3.01 to 2.25 GPa.

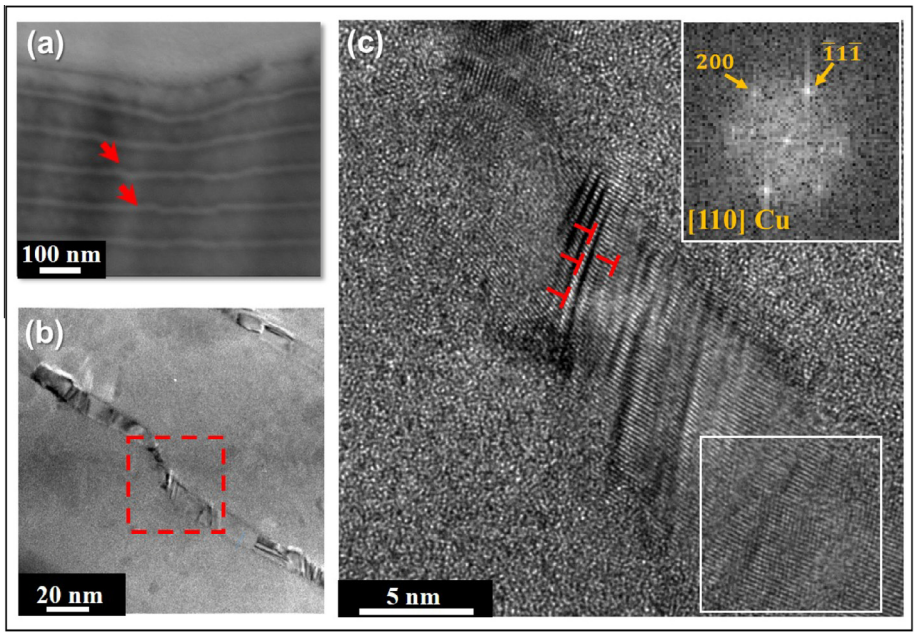

Fig. 4. Micrographs of a 100 nm amorphous CuZr/10 nm nc Cu nanolaminate (MS10) after 5 mN nanoindentation. (a) SEM backscattered electron image. The arrows show the plastic instabilities at necked regions in the Cu layers. (b) Bright field TEM images of a shear band region. (c) High resolution TEM image of the region marked red in (b), together with a FFT of the region marked in white. The location of several dislocations is indicated close to the necked region. (For interpretation of the references to color in this figure legend, the reader is referred to the web version of this article.)

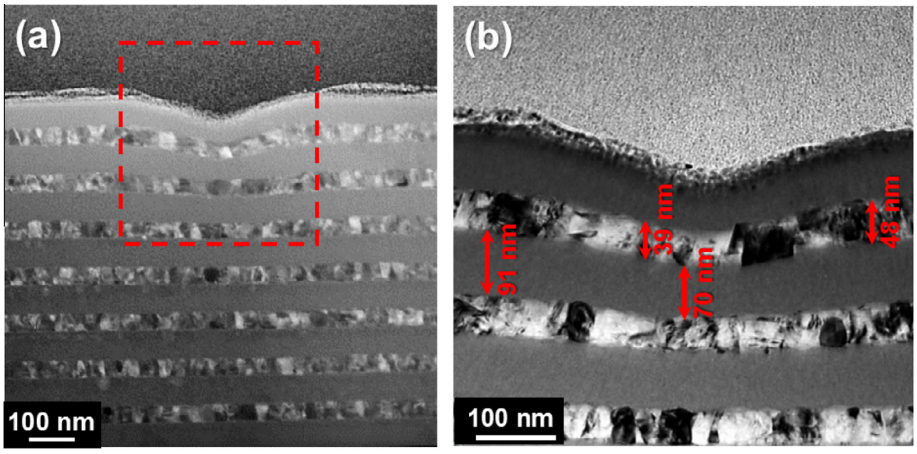

Fig. 5. TEM micrographs of a 100 nm CuZr/50 nm nc Cu nanolaminate (MS50) after 5 mN nanoindentation. (a) Dark field TEM micrograph. (b) Bright field TEM micrograph from the region marked in red in (a) showing co-deformation of both the amorphous CuZr layers and the nc Cu layers in the absence of visible shear bands. (For interpretation of the references to color in this figure legend, the reader is referred to the web version of this article.)

As the pillar diameter further shrinks to 300 nm, the flow stress increases to 2.62 GPa. The same trends are also observed in samples MS50 and MS100 when decreasing the pillar size from 2000 to 300 nm.

4. Discussion

4.1. Intrinsic size effects

4.1.1. Flow stress anisotropy and nanotwins

Fig. 10 summarizes the flow stress values obtained from both the pillar tests (using ~8% strain offset; symbols) and the nanoindentation tests where the flow stress was calculated as hardness/2.7 (dotted lines) [23]. The flow stress derived from indentation is smaller than the flow stress measured by uniaxial compression. A possible reason for this is the difference in strength of the hetero-interfaces when exposed to different types of stress states. If we correlate previous TEM observations with the hardness decrease upon increasing indentation depth, we conclude that the am/nc interface plane is relatively weak when exposed to shear. Hence, rotation of the interface regions may facilitate interfacial slip. The strain would then be localized inside the interface region, resulting in work-softening, such as observed for the nanolaminates at high strain.

Another possible explanation involves the {111} nanotwins that may contribute to out-of-plane

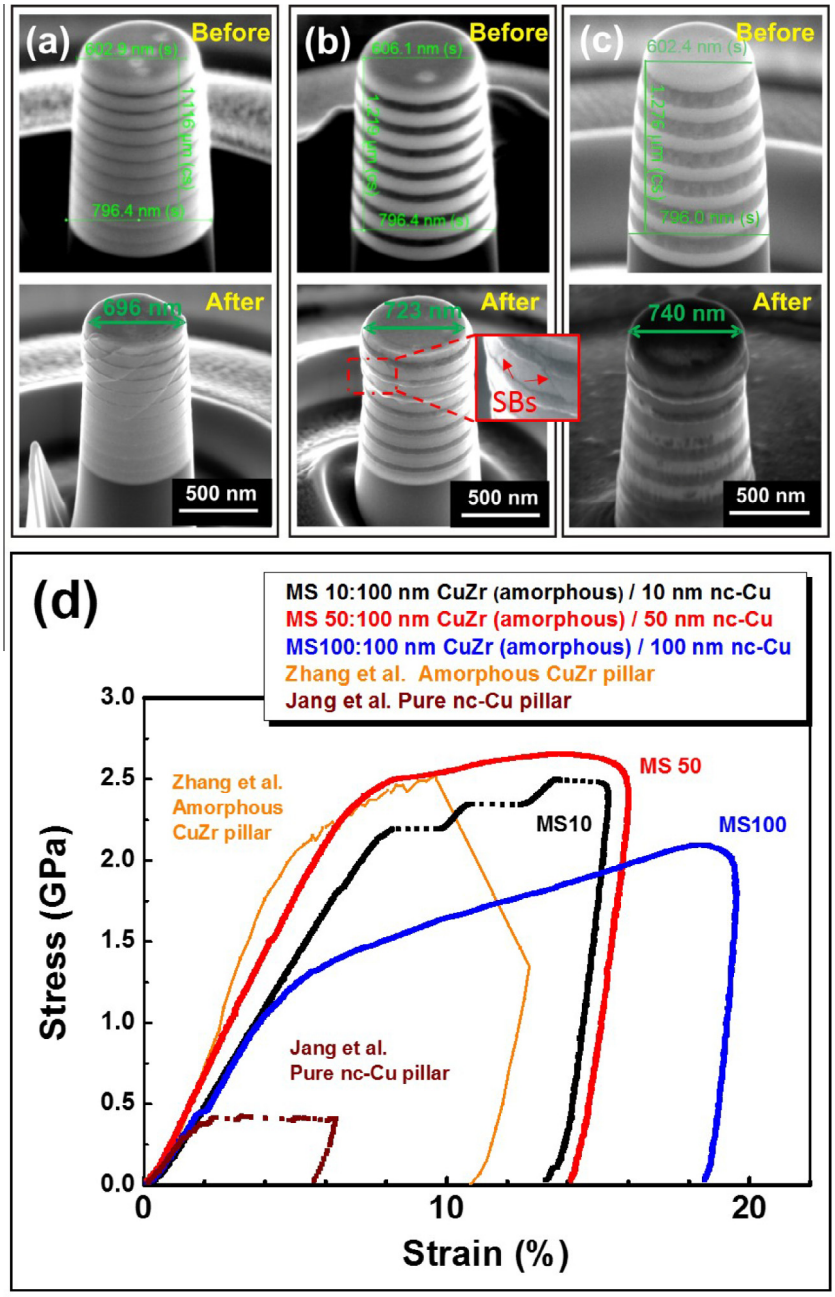

Fig. 6. (a–c) 52°-tilted SEM images of ~600 nm diameter pillars before and after compression. (a) 100 nm amorphous CuZr/10 nm nc Cu (MS10). (b) 100 nm amorphous CuZr/50 nm nc Cu (MS50). Note the shear bands indicated by red arrows in the inset. (c) 100 nm amorphous CuZr/100 nm nc Cu (MS100). (d) Corresponding stress–strain curves of the pillars compressed to 15–20% strain. Also shown in this figure are published stress–strain curves of amorphous CuZr [20] and nc Cu [37] compressed pillars with similar pillar diameter. (For interpretation of the references to colour in this figure legend, the reader is referred to the web version of this article.)

deformation in the as-deposited nc Cu layers. You et al. [39] studied nanotwin-induced plastic anisotropy in direct current electrodeposited nc Cu sheets by changing the loading direction with respect to the twin planes. They found that when the uniaxial stress was employed either perpendicular or parallel to the twin planes, it would trigger a "hard mode" slip situation, where the dislocation slip plane is inclined towards the twin boundaries and hence dislocations experience higher flow resistance, Fig. 11. However, if the loading direction is 45° relative to the twin boundary plane, "soft mode" slip is enabled, where dislocations move parallel to the twin boundaries, leading to a low flow stress. Such anisotropy associated with dislocation slip in nc Cu was also reported elsewhere [40–42]. In the current uniaxial compression tests, when the compression axis is perpendicular to the {111} twin boundaries, the $\{111\}\langle 110\rangle$ hard mode slip is active, i.e. twin boundaries tend to act as slip barriers against dislocation glide. In our Berkovich nanoindentation tests, the 65.3° tool angle promotes a higher load component at

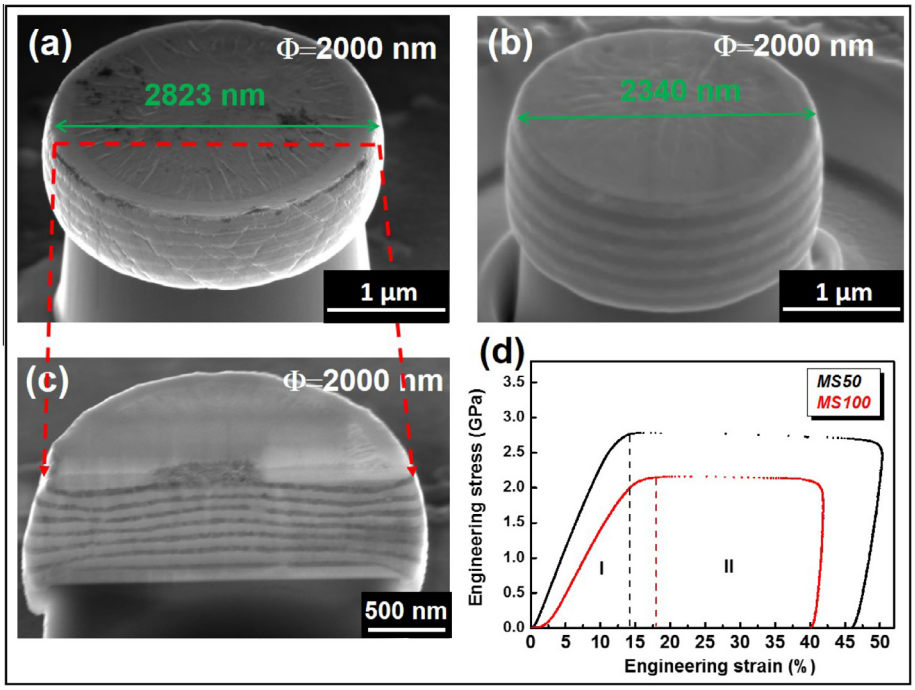

Fig. 7. (a–c) 52°-tilted SEM images of ~2 μm diameter pillars after compression. (a) 100 nm amorphous CuZr/50 nm nc Cu (MS50). (b) 100 nm amorphous CuZr/100 nm nc Cu (MS100). (c) Cross-section view of MS50 after compression cut approximately at the location indicated in (a). (d) Corresponding stress–strain curves of pillars compressed to 40–50% strain. Note that the fracture strain of these two laminates would be higher based on the SEM morphology.

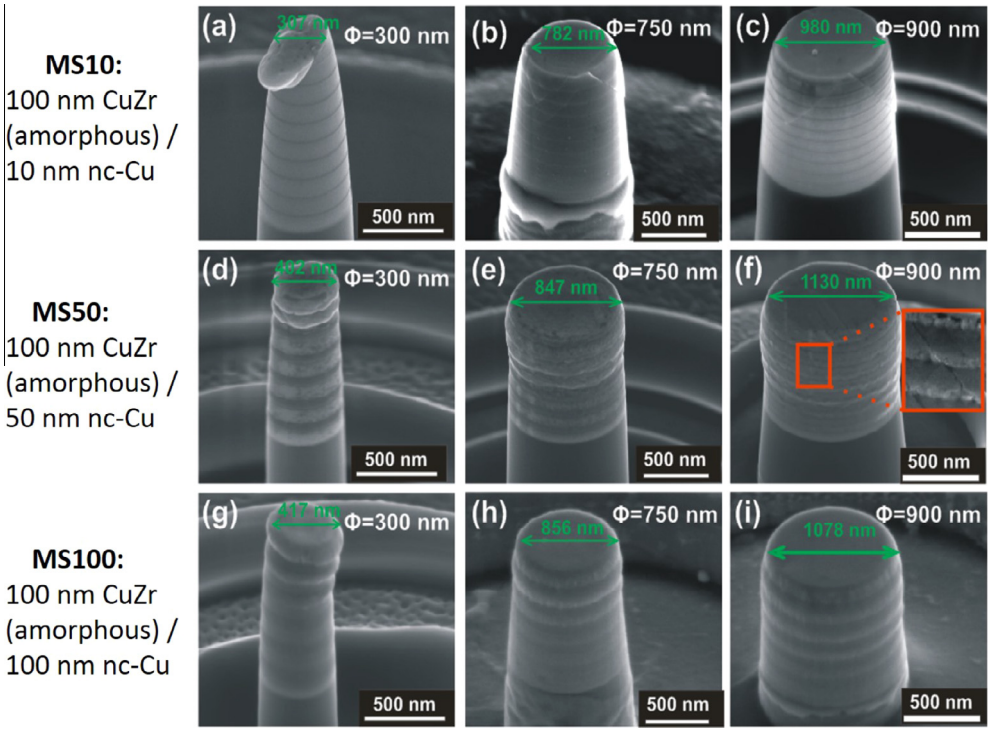

Fig. 8. Representative 52°-tilted SEM images of pillars after 15–20% strain in uniaxial compression test. (a–c) MS10 (100 nm amorphous CuZr/10 nm nc Cu) pillars with different diameters show shear deformation with a limited number of shear bands. (d–f) MS50 (100 nm amorphous CuZr/50 nm nc Cu) pillars show a transition from slight extrusion of Cu layers to co-deformation of both CuZr and Cu layers as the pillar size increases. (g–i) MS100 (100 nm amorphous CuZr/100 nm nc Cu) pillars exhibit the same trend as MS50. However, no shear bands are visible in the amorphous CuZr layers.

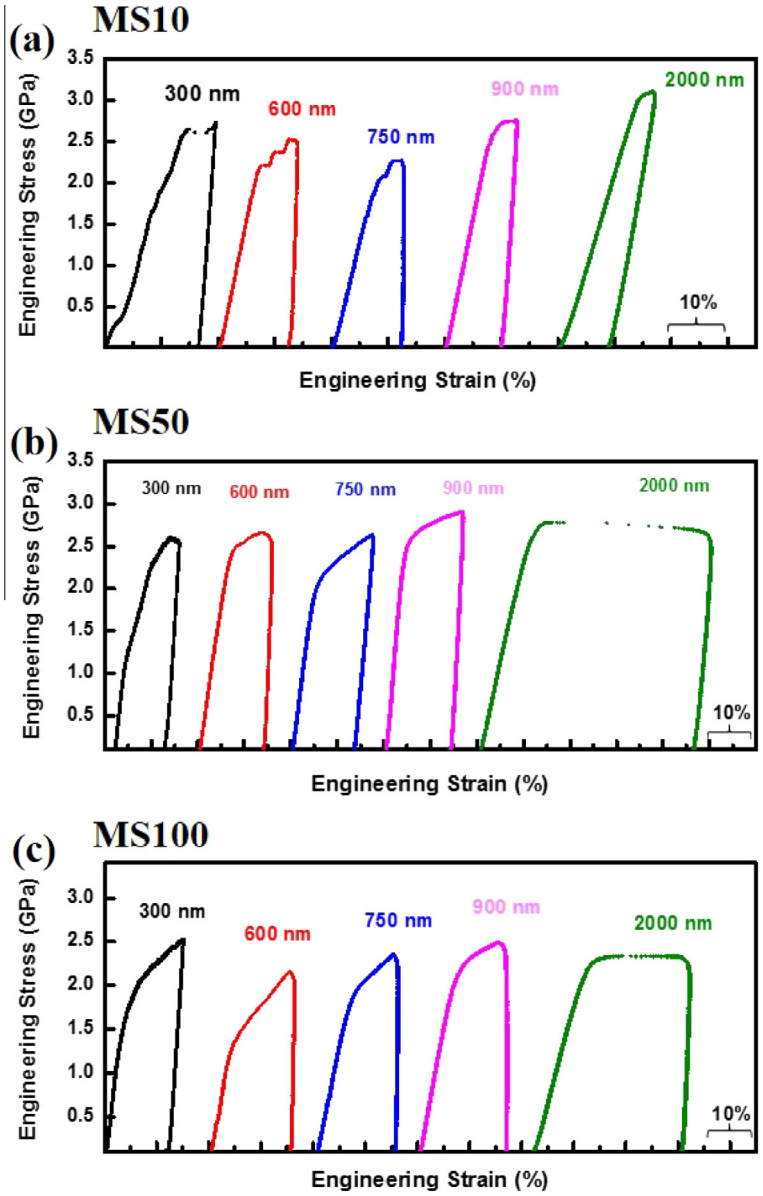

Fig. 9. Engineering stress–strain curves for pillars with different extrinsic and intrinsic size scales. (a) MS10 (100 nm amorphous CuZr/10 nm nc Cu) pillars. (b) MS50 (100 nm amorphous CuZr/50 nm nc Cu) pillars. (c) MS100 (100 nm amorphous CuZr/100 nm nc Cu) pillars. The numbers above the curves indicate the pillar diameters before deformation. Note that the curves have been shifted along the abscissa for improved clarity.

45° to the twin boundary plane, so that "soft mode" dislocation slip is favored. Then, more dislocations glide along the twin boundaries instead of being blocked by them. Hence, dislocation glide in the nc Cu layers is easier in nanoindentation than under uniaxial compression, Fig. 10.

Fig. 11 gives an example of the nanotwin alignment and of the high nanotwin density observed inside the Cu layer in sample MS10. The average twin spacing amounts to $\sim 5 \pm 2$ nm in samples MS10 and MS50 and 7 ± 3 nm in sample MS100. This means that the nanotwin spacing does not change substantially with the Cu layer thickness. This is plausible since the same deposition conditions were employed for all samples.

4.1.2. Confined layered slip and effect of Cu layer thickness

The high flow stress of am/crystalline nanolaminates results in part from the hetero-interfaces confining dislocation slip inside the nc Cu layers. In laminates composed of soft/ductile layers and hard/brittle phases, plastic flow is initially governed by the soft/ductile phase [23,43,44]. In the present case, the stress required by a single dislocation for gliding inside one of the Cu layers can be expressed through the confined layer slip (CLS) model as:

$$\sigma_{cls} = M\frac{\mu^* b}{8\pi h'}\left(\frac{4-\nu}{1-\nu}\right) ln\frac{ah'}{b} - \frac{f}{h} + \frac{\mu^* b}{L(1-\nu)} \qquad (2)$$

where $M \approx 3.7$ is the Taylor factor of the {111} textured Cu, h is the Cu layer thickness, $h' = \frac{h}{sin\theta}$ is the thickness of

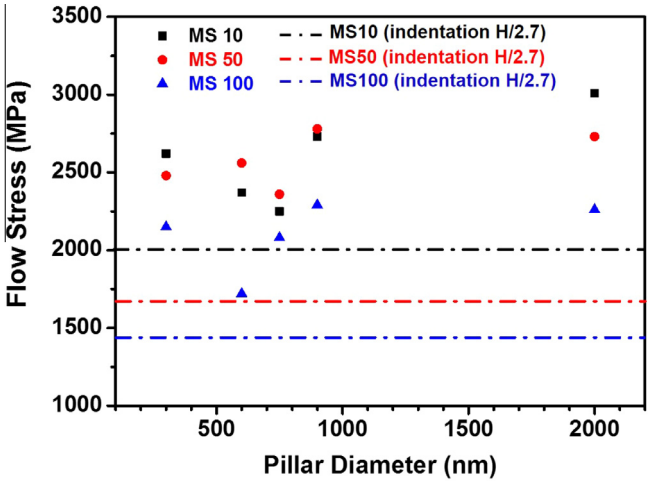

Fig. 10. Dependence of flow stress on extrinsic and intrinsic size effects in amorphous CuZr/nc Cu nanolaminates. The flow stress values were obtained both from the pillar tests (~8% strain offset; full symbols) and also from nanoindentation tests, where the flow stress was calculated as hardness/2.7 (dotted lines). We studied three different materials systems: MS10 (100 nm amorphous CuZr/10 nm nc Cu), MS50 (100 nm amorphous CuZr/50 nm nc Cu) and MS100 (100 nm amorphous CuZr/100 nm nc Cu). The samples exhibit no extrinsic pillar size effect.

the layer parallel to the glide plane, θ is the angle between the slip plane and the interface, $b = \sim 0.2556$ nm is the magnitude of the Burgers vector, $\nu \sim 0.343$ is the Poisson ratio of Cu and μ^* is the effective shear modulus of the (111) Cu layer. The geometrical factor $\alpha \approx 0$–1 represents the core cut-off parameter and contains the contribution of the extrinsic size constraint effect on the layer strength; is the mean spacing of glide loops in a parallel array; and $f \approx 0.5$–1.1 J m^{-2} is the characteristic am/crystalline interface stress [45]. When inserting $\alpha = 0.6$, $L = 12.5$ nm, $\mu^* = 30.6$ GPa and $f = 0.6$ J m^{-2} into Eq. (2), a stress level as shown in Table 2 results for the CLS model. The predicted values, 2.38 GPa for sample MS50 and 2.00 GPa for MS100, generally agree with the flow stress measured in the pillar compression tests. However, the value suggested by the CLS model for sample MS10 is 4.40 GPa, i.e. it strongly overestimates the flow stress level observed experimentally, namely, 2.37–3.01 GPa. We interpret this deviation in terms of a transition from the dislocation-dominated CLS mechanism for the case of the thicker Cu layers to a co-deformation mechanism where shear band penetration initiated by the amorphous phase prevails when the Cu layer thickness is reduced down to 10 nm. This means that those samples with the largest volume fraction of amorphous phase are prone to develop shear bands that can more easily intersect numerous nc Cu layers. When increasing the nc Cu layer thickness, however, such multi-layer penetration of shear bands is reduced [46]. Therefore, we propose that the MS10 specimens are prone to develop shear bands that penetrate numerous layers. The morphology of such shear bands is parallel to those observed in monolithic metallic glasses. Generally, the Cu layers are deformed by dislocation glide and get thinned to a few nanometers (cf. Fig. 4b). Such a process may even alter the local structures and induce mechanical alloying of the shear banded regions, as will be discussed in more detail below [47,48].

4.1.3. Shear banding and Cu layer thickness

Kim et al. [22] investigated CuZr/polyisoprene nanolaminates by micropillar compression tests and suggested that the soft polyisoprene layers may act as stress absorbers and dissipate or redistribute the localized stress of the shear bands coming from the metallic glass layers. In the present study, the mechanism of suppressing catastrophic shear banding is similar: highly localized stresses arising from confined early stage shear bands may be partially absorbed by the abutting Cu layers and hence be accommodated by co-deforming the Cu layers. In our experimental set-up we had strictly controlled the amorphous layer thickness to remain constant while that of the Cu layers varied between 10 and 100 nm. The suppression of shear bands and the absence of strain bursts in Fig. 6 clearly reveal that thicker Cu layers are indeed more efficient in arresting emerging

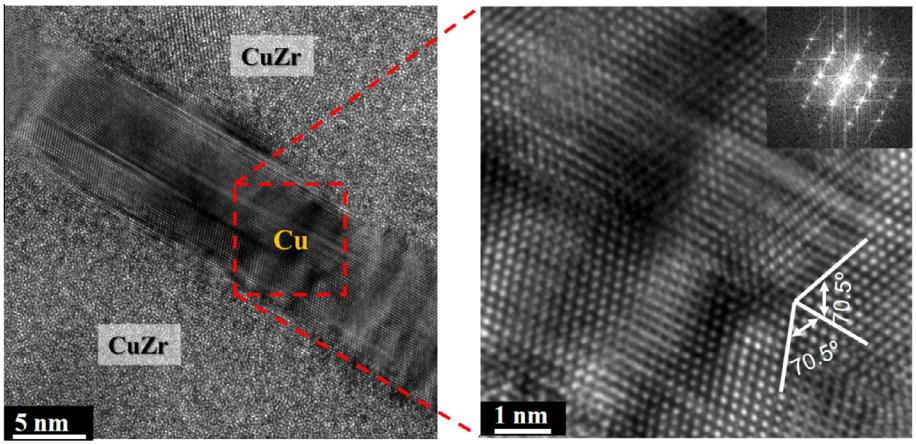

Fig. 11. Example of the nanotwin alignment and of the high nanotwin density observed by TEM inside the Cu layer in sample MS10. The average twin spacing amounts to $\sim 5 \pm 2$ nm in samples MS10 and MS50 and 7 ± 3 nm in sample MS100 (MS10: 100 nm amorphous CuZr/10 nm nc Cu; MS50: 100 nm amorphous CuZr/50 nm nc Cu; MS100: 100 nm amorphous CuZr/100 nm nc Cu).

Table 2
Comparison between CLS calculated flow stress values (cf. Eq. (2)) for the crystalline Cu layers and the pillar flow stress values obtained from uniaxial compression experiments. MS10 (100 nm amorphous CuZr/10 nm nc Cu); MS50 (100 nm amorphous CuZr/50 nm nc Cu); and MS100 (100 nm amorphous CuZr/100 nm nc Cu).

Material system	MS10	MS50	MS100
Cu layer flow stress calculated by CLS model (GPa)	4.40	2.38	2.00
Flow stress from uniaxial pillar compression (GPa)	2.37–3.01	2.36–2.78	1.72–2.29

shear bands. More confined, i.e. localized shear bands have to be formed if larger shear bands cannot penetrate through the Cu layers. The instability associated with the nucleation and expansion of large shear bands that penetrate multiple layers will thus be suppressed since the imposed load is dissipated in the form of a high dispersion of more confined shear bands. Thus, the strain bursts observed in the load-controlled experiments are weaker compared to those observed in homophase metallic glasses. Finally, in all interpretations it has to be considered that the tapered geometry of the pillars is associated with a stress decrease from top to bottom so that mechanical inhomogeneity cannot be entirely excluded.

4.2. Extrinsic effects

A previous work [18] on Cu/CuZr crystalline/amorphous nanolaminates with equal amorphous and nc layer thicknesses between 5 and 50 nm analyzed the compression of pillars between 325 and 1425 nm diameter. The yield strength data presented in this paper reveal a "smaller is stronger" trend.

In order to check such effects in the present study, we calculated the flow stress values based on the topmost diameter, for avoiding underestimation of the pillar flow stresses. However, as shown in Fig. 10, no extrinsic size effect can be observed when the pillar diameters are reduced from 2000 to 300 nm for all three multilayer systems. This finding is in contrast to observations made in a previous work: CuZr/Cu multilayered samples with a 5 nm thickness period were reported to exhibit a yield strength of 4.8 GPa for $\Phi = 350$ nm pillars and of 3 GPa for $\Phi = 1425$ nm pillars [18]. One reason for this difference is that in the previous study [18] smaller layer thicknesses were used (down to 5 nm). Another reason is that in our current samples we use unequal layer thicknesses for the two phases while the previous work used equal layer thicknesses. One should also note that systematic scattering always occurs for pillar tests at sub-micron scales, which may resemble a size effect. This means that pronounced extrinsic size effects are not observed among our three multilayered samples.

4.3. Transition in deformation mode

4.3.1. 1 Flow stress vs. linear rule-of-mixture

As a lower bound estimate, i.e. neglecting the hetero-interface strengthening, we approximate the flow stress of the laminates by a linear rule-of-mixtures [49–51]:

$$\sigma_{NL} = \sigma_a \frac{t_a}{t_a + t_{nc}} + \sigma_{nc} \frac{t_{nc}}{t_a + t_{nc}} \tag{3}$$

where σ_{NL} describes the lower bound flow stress of the compound, $\sigma_a = 2370$ MPa is the flow stress of the amorphous CuZr layer [9], $\sigma_{nc} = 920$ MPa is the flow stress of pure nc Cu, as calculated from previous reports of pure electrodeposited nc Cu [52,53] and t_a and t_{nc} are the thickness of the amorphous and nc layers, respectively.

The observed flow stress values exceed the linear rule-of-mixture approximation for all multilayered samples: For the MS10 specimens we found an experimental range of 2370–3010 MPa for the flow stress, which roughly matches the lower bound value suggested by the linear rule-of-mixtures, i.e. 2240 MPa, Fig. 12. For the MS50 specimens the linear rule-of-mixtures suggests only 1887 MPa for the flow stress, underestimating the experimentally observed strength of the pillar samples which fall into the range 2360–2780 MPa, Fig. 12. We attribute this to the large scatter of the experimental data. For the MS100 specimens the values are 1720–2290 MPa vs. 1645 MPa predicted as lower bound by the linear rule-of-mixtures.

4.3.2. Transition in deformation mode depending on layer thickness

When the thickness of the Cu layer is only 10 nm (MS10), dislocation slip inside the nc Cu layers cannot accommodate the imposed strain intrinsically. Therefore, these thin Cu layers cannot easily prevent the cross-phase propagation of shear bands stemming from the amorphous CuZr layers. The stress concentration acting on the amorphous/crystalline interfaces leads to a localized dislocation flux along the path of the shear band [46]. The dislocations, when crossing the CuZr/Cu interfaces, will drag Cu atoms into the CuZr layer, leading to chemical mixing [54] and even local amorphization of the crystalline layer. The deformation of the MS10 samples is hence dominated by amorphous shear banding and its cross-phase percolation, Fig. 12.

When increasing the Cu layer thickness to 100 nm (MS100), pillar deformation is initially practically only carried by the Cu layers, due to their lower initial flow stress compared to that of the amorphous CuZr layers. Conventional plastic deformation mechanisms, such as dislocation multiplication, intra-phase glide and pile-up-induced work-hardening, first dominate the Cu deformation. As deformation proceeds, the flow stress in the nc Cu layers hence rapidly approaches that of the metallic glass layers due to intra-layer strain hardening.

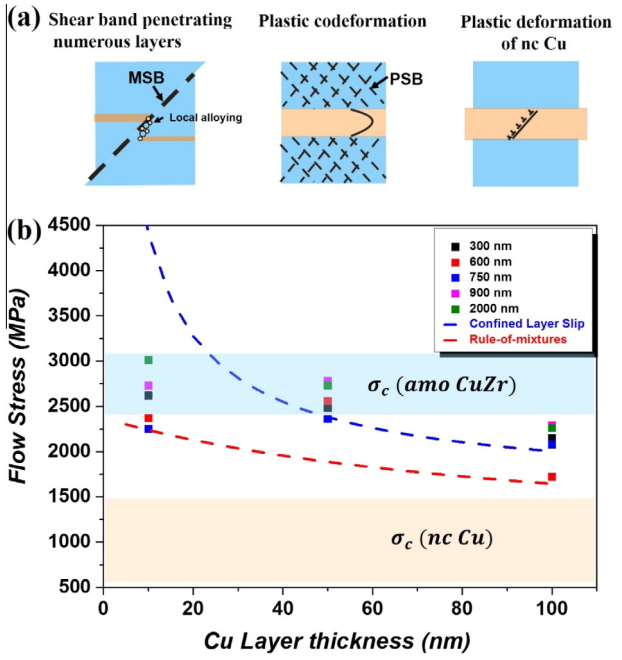

Fig. 12. (a) Schematic illustration of the deformation mechanism in the metallic amorphous/crystalline nanolaminates as a function of Cu layer thickness (MSB: mature shear band penetrating multiple layers; PSB: preliminary (confined) shear band). (b) The data are taken from Fig. 10, here plotted as a function of the Cu layer thickness, together with two model predictions (confined layer slip: blue dotted line; linear rule of mixture: red dotted line) as well as the range of expected flow stress values for pure amorphous CuZr and pure nc Cu. (For interpretation of the references to color in this figure legend, the reader is referred to the web version of this article.)

When the Cu layers assume an "ideal" thickness, such as 50 nm, as observed here, the effect of plastic co-deformation on the strength increase is even more pronounced since the strengthening potential of both layer types is ideally coupled. The CuZr metallic glass layers sustain considerable intrinsic, i.e. intra-phase, plasticity via shear banding which, however, remains confined inside the layers. The Cu layers can further dissipate these localized loads, such as originating from the incoming confined shear bands, by intrinsic plastic deformation without strong localization. Due to the coupled deformation mechanisms of the Cu layers and the metallic glass layers, a strong and yet ductile mechanical response can be achieved in the MS50 samples. A proper design and sequence of the laminate architecture seem thus to be crucial for the enhancement of the mechanical properties by utilizing these different mechanisms simultaneously.

4.3.3. Influence of the am/nc interfaces on dislocation motion

The influence of the am/nc hetero-interfaces on dislocation motion inside the Cu is two-fold. At low strains, the debris from elongated expanding dislocation loops get deposited at the hetero-interfaces. Reactions with inclined dislocations produce dislocations with Burgers vectors in the interface plane, i.e. interfacial dislocations [23]. The interfacial dislocations can move along the interface and dissipate localized strains induced by the small shear bands from the amorphous CuZr layer. The CuZr/Cu interfaces serve as barriers against dislocations, promoting work-hardening of the Cu. When the nanolaminate is deformed further, the interface, according to previous molecular dynamics simulations [21], may in turn attract dislocations, drawing them into it, thus reducing the dislocation density [46], Fig. 4. Therefore, such am/nc interfaces may reveal better strain dissipation potential compared to crystalline/crystalline interfaces since the incoming strain from the amorphous phase is not limited by fixed Burgers vectors and slip planes. Instead, omnidirectional atomic motions and shear transformation zones can facilitate both dislocation movement in the crystal and inelastic shear/dislocation shuffling among the layers [55]. Such interface controlled co-deformation mechanisms also lead to structural/chemical mixing at higher deformations (mechanical alloying), which will be discussed elsewhere [54].

The analysis also shows that both extrinsic size effects (pillar size, taper, loading type, tool design, compression vs. indentation, surface-to-volume ratio etc. [31,56–62]) and intrinsic size effects (intra-layer substructure, layer thickness, interface structure) should be jointly considered when interpreting mechanical size effects in nanolaminates, specifically possible transitions in the co-deformation mode.

5. Conclusions

We synthesized multilayer nanolaminates consisting of alternating layers of amorphous $Cu_{54}Zr_{46}$ and nc Cu by direct current sputtering. The probed combinations were based on 100 nm CuZr amorphous layers and nc Cu layers of varying thickness (10, 50 and 100 nm). Loading was exerted by nanoindentation and pillar compression. The main findings are as follows:

1. An increase in Cu layer thickness can suppress catastrophic propagation of shear bands. For 10 nm Cu layers, small confined shear bands can readily develop into larger, i.e. percolative shear bands. For 50 and 100 nm thick Cu layers a higher fraction of confined shear bands forms in the amorphous layers at low strains (10%), distributing the load more homogeneously. Generally, the interplay of shear bands with the crystalline Cu layers increases the compound's toughness and ductility.
2. In the three multilayer systems studied here, the experimentally observed compressive flow strength of the submicron/micron pillars exceeds the lower bounds given by a linear rule-of-mixture approximation. Specially, the MS50 pillars not only have flow stresses (2.57 ± 0.21 GPa) that match the value of pure CuZr metallic glass, but also accommodate high compressive plastic strains (>40%) by the confinement of small shear bands inside the metallic glass layers. This composite behavior reveals a path to design am/nc composite

structures that are "strong and ductile" by utilizing the cooperation of the deformation modes in the two different types of layers.
3. Decreasing the pillar diameter from 2000 to 300 nm shows no obvious extrinsic size effect among the three types of multilayer systems. Both extrinsic and intrinsic influence factors should be generally considered when interpreting apparent mechanical size effects.
4. The "confined layer" dislocation slip mode well explains the flow stress of Cu in the 100/50 and 100/100 nm CuZr/Cu nanolaminates but overestimates the flow stress in the 100/10 nm CuZr/Cu nanolaminates, where shear band penetration prevails the nanolaminate co-deformation.

Acknowledgments

The authors are grateful to Dr A. Kostka for help with the TEM experiments. W.G. acknowledges the IMPRS-SurMat School scholarship. J.H.Y. acknowledges support by the Alexander von Humboldt Foundation. V.M. and S.K. gratefully acknowledge the funding of the German Research Council (DFG), which, within the framework of its "Excellence Initiative", supports the Cluster of Excellence "Engineering of Advanced Materials" at the University of Erlangen-Nürnberg.

References

[1] Hofmann DC. Science 2010;329:1294.
[2] Donovan PE, Stobbs WM. Acta Metall 1981;29:1419.
[3] Schuh C, Hufnagel T, Ramamurty U. Acta Mater 2007;55:4067.
[4] Yoshizawa Y, Oguma S, Yamauchi K. J Appl Phys 1988;64:6044.
[5] Pardo A, Merino M, Otero E, Lopez M, Mhich A. J Non-Cryst Solids 2006;352:3179.
[6] Zhang C, Zhang H, Lv M, Hu Z. J Non-Cryst Solids 2010;356:1703.
[7] Li R, Liu G, Stoica M, Eckert J. Intermetallics 2010;18:134.
[8] Ashby M, Greer A. Scripta Mater 2006;54:321.
[9] Wang ZT, Zeng KY, Li Y. Scripta Mater 2011;65:747.
[10] Hays CC, Kim CP, Johnson WL. Phys Rev Lett 2000;84:2901.
[11] Wu Y, Xiao Y, Chen G, Liu CT, Lu Z. Adv Mater 2010;22:2770.
[12] Conner RD, Johnson WL, Paton NE, Nix WB. J Appl Phys 2003;94:904.
[13] Wu WF, Li Y, Schuh CA. Philos Mag 2008;88:71.
[14] Bei H, Xie S, George EP. Phys Rev Lett 2006;96:105503.
[15] Wang CC, Ding J, Cheng YQ, Wan JC, Tian L, Sun J, et al. Acta Mater 2012;60:5370.
[16] Jang DC, Greer JR. Nat Mater 2010;9:215.
[17] Jang D, Greer JR. Scripta Mater 2011;64:77.
[18] Zhang JY, Liu G, Lei SY, Niu JJ, Sun J. Acta Mater 2012;60:7183.
[19] Liu MC, Du XH, Lin IC, Pei HJ, Huang JC. Intermetallics 2012;30:30.
[20] Kim JY, Jang D, Greer JR. Adv Funct Mater 2011;21:4550.
[21] Wang Y, Li J, Hamza AV, Barbee Jr TW. Proc Natl Acad Sci USA 2007;104:11155.
[22] Kim JY, Gu X, Wraith M, Uhl JT, Dahmen KA, Greer JR. Adv Funct Mater 2012;22:1972.
[23] Misra A, Hirth JP, Hoagland RG. Acta Mater 2005;53:4817.
[24] Oliver WC, Pharr GM. J Mater Res 1992;7:1564.
[25] Hopcroft MA, Nix WD, Kenny TW. J Microelectromech Syst 2010;19:229.
[26] Gan L, BenNissan B, BenDavid A. Thin Solid Films 1996;290:362.
[27] Sanders PG, Eastman JA, Weertman JR. Acta Mater 1997;45:4019.
[28] Das J, Tang M, Kim K, Theissmann R, Baier F, Wang W, et al. Phys Rev Lett 2005;94:205501.
[29] King RB, Int J. Solids Struct 1987;23:1657.
[30] Frick CP, Clark BG, Orso S, Schneider AS, Arzt E. Mat Sci Eng A-Struct 2008;489:319.
[31] Volkert CA, Lilleodden ET. Philos Mag 2006;86:5567.
[32] Spear KE, Dismukes JP. Synthetic diamond: emerging CVD science and technology. New York: Wiley; 1994.
[33] Zhang JY, Zhang P, Wang RH, Liu G, Zhang GJ, Sun J. Mat Sci Eng A – Struct 2012;554:116.
[34] Lefloch A. Philos Mag 1969;19:429.
[35] Jang DC, Cai C, Greer JR. Nano Lett 2011;11:1743.
[36] Uchic MD, Shade PA, Dimiduk DM. Ann Rev Mater Res 2009;39:361.
[37] Pampillo CA, Chen HS. Mater Sci Eng 1974;13:181.
[38] Maass R, Klaumunzer D, Löffler JF. Acta Mater 2011;59:3205.
[39] You Z, Li X, Gui L, Lu Q, Zhu T, Gao H, et al. Acta Mater 2013;61:217.
[40] Dao M, Lu L, Shen YF, Suresh S. Acta Mater 2006;54:5421.
[41] Dao M, Lu L, Asaro R, Dehosson J, Ma E. Acta Mater 2007;55:4041.
[42] Lu K, Lu L, Suresh S. Science 2009;324:349.
[43] Li N, Wang J, Misra A, Huang JY. Microsc Microanal 2012;18:1155.
[44] Zhang JY, Lei S, Liu Y, Niu JJ, Chen Y, Liu G, et al. Acta Mater 2012;60:1610.
[45] Cammarata RC. Prog Surf Sci 1994;46:1.
[46] Pekarskaya E, Kim CP, Johnson WL. J Mater Res 2001;16:2513.
[47] Raabe D, Ohsaki S, Hono K. Acta Mater 2009;57:5254.
[48] Raabe D, Choi PP, Li YJ, Kostka A, Sauvage X, Lecouturier F, et al. Mrs Bull 2010;35:982.
[49] Hangen U, Raabe D. Acta Metall Mater 1995;43:4075.
[50] Raabe D, Heringhaus F, Hangen U, Gottstein G. Z Metallk 1995;86:416.
[51] Raabe D, Mattissen D. Acta Mater 1998;46:5973.
[52] Lu L, Shen YF, Chen XH, Qian LH, Lu K. Science 2004;304:422.
[53] Lu L, Chen X, Huang X, Lu K. Science 2009;323:607.
[54] Guo W, Jägle EA, Choi PP, Yao J, Kostka A, Schneider JM, Raabe D. Phys Rev Lett 2014;113:069903. http://dx.doi.org/10.1103/PhysRevLett.113.069903.
[55] Wang YM, Hamza AV, Barbee TW. Appl Phys Lett 2007;91:061924.
[56] Maass R, Van Petegem S, Ma DC, Zimmermann J, Grolimund D, Roters F, et al. Acta Mater 2009;57:5996.
[57] Raabe D, Ma D, Roters F. Acta Mater 2007;55:4567.
[58] Zaafarani N, Raabe D, Singh RN, Roters F, Zaefferer S. Acta Mater 2006;54:1863.
[59] Zaafarani N, Raabe D, Roters F, Zaefferer S. Acta Mater 2008;56:31.
[60] Uchic MD, Dimiduk DM, Florando JN, Nix WD. Science 2004;305:986.
[61] Greer JR, Oliver WC, Nix WD. Acta Mater 2005;53:1821.
[62] Nix WD, Greer JR, Feng G, Lilleodden ET. Thin Solid Films 2007;515:3152–7.